Hindawi
Applied Bionics and Biomechanics
Volume 2024, Article ID 6637846, 13 pages
https://doi.org/10.1155/2024/6637846

Research Article

Nanoparticle Delivery in Microvascular after Cerebral Ischemia: A Simulation Study

Peiqian Chen[1], **Bing Dong**[2] and **Weiwu Yao**[1]

[1]*Department of Imaging, Tongren Hospital, Shanghai Jiao Tong University School of Medicine, Shanghai 200336, China*
[2]*School of Nuclear Science and Engineering, Shanghai Jiao Tong University, Shanghai 200240, China*

Correspondence should be addressed to Weiwu Yao; yaoweiwuhuan@163.com

Received 23 December 2022; Revised 23 January 2024; Accepted 25 January 2024; Published 7 February 2024

Academic Editor: Raimondo Penta

Nanodrug delivery systems have been used in the diagnosis and treatment of ischemic stroke. However, the delivery mechanisms of nanoparticles within microvascular after cerebral ischemia have not been systematically revealed. This study aims to investigate the binding of different nanoparticles to the walls of ischemic brain microvascular through numerical simulations. In this study, 3D models of cerebral microvascular based on ischemic pathological changes are constructed. After building the mesh of microvascular, computational fluid dynamics is used to simulate blood flow and nanoparticle delivery. The simulation results show that the total amount of binding nanoparticles with small size is higher than that with large size. The large-sized nanoparticles are more easily delivered to the stenosis. The density of the nanoparticles has no significant effect on delivery. Furthermore, the study finds that the presence of red blood cells can significantly enhance the delivery efficiency of nanoparticles. In addition to evaluating the forces exerted on the nanoparticles, the impact of the binding affinity of the modified ligand on nanoparticles to the target receptor on delivery is investigated. In summary, selecting suitable nanoparticles according to different targets will improve the delivery efficiency of nanodrugs. The microvascular delivery model of nanoparticles proposed in this study may be helpful in the design of nanoparticles for diagnosis and treatment of cerebral ischemia.

1. Introduction

Stroke is the leading cause of disability in adults worldwide and the second leading cause of cardiovascular diseases-related mortality, of which ischemic stroke accounts for 80%–90% [1, 2]. The number of stroke patients continues to increase as the population increases and society ages. The development of stroke drugs has been going on, such as thrombolytic drugs and neuroprotective agents. However, many new drugs that have shown promising therapeutic effects in preclinical trials are not available to the market due to poor clinical efficacy and low safety. The excellent and unique properties of nanoparticles (NPs) enable them to be widely studied and applied in various fields of life, such as catalysts [3], computer architecture [4], water purification [5], antibacterial materials [6], and surface-enhanced Raman spectroscopy detection [7]. In medicine, nanodrug delivery systems have attracted much attention due to their advantages including high drug loading, targetability, improved pharmacokinetics, and good biocompatibility. A variety of nanodrug delivery systems that can be used as diagnostic or therapeutic tools have been used in preclinical studies of ischemic stroke [8–12]. These studies include a variety of nanocarriers with different modifications, providing a variety of solutions to the difficulties of drug delivery in cerebral ischemia. However, due to the lack of comparison, it is difficult to determine which nanodrug delivery system is more suitable for the diagnosis and treatment of cerebral ischemia. Thus, systematical comparison among different nanodrug delivery systems is necessary. In addition, a series of pathological changes occur in the microcirculation after cerebral ischemia, and these changes inevitably affect the delivery of NPs. Understanding how these changes affect NP delivery will be of great help in improving the efficiency of nanomedicine delivery, but these changes are difficult to observe directly by experiment. Numerical simulation is an alternative method that can systematically study the NPs delivery, having the advantages of low cost, high speed, and precision, and

most importantly, it can help us deeply understand experimental phenomena.

Benefited from the advancement of numerical simulation and the substantial increase in the speed of computers, computational fluid dynamics (CFD) become a powerful tool to study biologically relevant flows. In terms of nanodrug delivery, numerical simulations are mostly used to study particle delivery in tumor tissues, main artery and microvascular [13–15]. In which, drug delivery in microvascular is most of the concern. This study focused on the delivery of NP in microvascular. There have been many studies of NP delivery in microvascular. Tan et al. [16] found that NPs with smaller size and rod shape have higher binding capabilities as a result of smaller drag force and larger contact area, and the strength of NPs binding decreases with increased shear rate. Liu et al. [17] found that shear rate in microvascular has an important influence on the diffusion of NPs. Yue et al. [18] found that a change in blood flow velocity distribution can increase the margination probability of NPs to the vessel wall, thereby enhancing their adhesion to the target area. It can be seen that the transportation of NPs in microvascular are affected by multiple factors. However, most studies of NP delivery in microvascular use lumens with very simple geometries, usually 2D or 3D single or Y-shaped channels with varying diameters. This is far from the real microvascular network and does not reflect the influence of the geometry of the vessel network on NP delivery. In addition, the microvascular network in the pathological state is different from that in the normal state. Numerical simulations of specific pathological states can more accurately reveal the mechanisms of NP delivery in this state, which is more helpful for drug development and clinical transformation.

This study focuses on NP delivery in capillaries after cerebral ischemia. In this study, 3D models of microvascular are established based on the electron microscope parameters of rat cerebral cortex capillaries and the research on blood flow regulation of cerebral microvascular. NPs with different sizes and densities are released into the models to simulate flow and binding to the vessel wall. The delivery mechanisms of NPs in ischemic brain microvascular are revealed by analyzing the hemodynamic changes, the size and density of NPs, the force exerted on NPs, the association coefficient of the ligand–receptor pairs that modify the NPs, and the impact of the presence or absence of red blood cells (RBCs) on the binding of NPs to the vessel wall. This study aims to provide help for the optimal design of NPs for the diagnosis and treatment of cerebral ischemia.

2. Materials and Methods

2.1. Geometry and Mesh of Microvascular. Hill et al. [19] used optical imaging technology to investigate the regulation at various sites on the vascular tree in living mice and found that the regulation of cerebral blood flow under physiological and pathological conditions is mediated by arteriole smooth muscle cells (SMCs), rather than capillary pericytes. After cerebral ischemia, capillaries undergo a series of changes

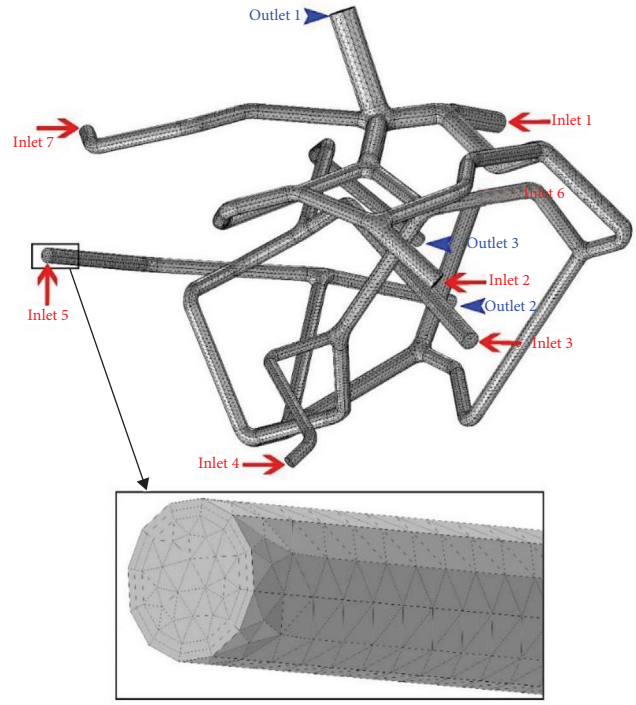

Figure 1: Schematic view of tetrahedral mesh used in the CFD simulation. Inside the black frame is an enlarged view of the vessel mesh.

due to the constriction of terminal SMCs, from no obvious changes, to local stenosis of the lumen, and then to lumen obstruction. Based on the above pathological changes after ischemia, there are three geometric models in this study: normal model, stenosis model, and occlusion model. The 3D geometric models of microvascular are constructed by SOLIDWORKS. The normal model of microvascular comes from Secomb et al.'s [20] research, which is derived from electron microscope images of a rat cerebral cortex. First, the microvascular network skeleton is established based on the coordinates of the blood vessel segments, then two adjacent tubular blood vessel segments are constructed and connected through curved surfaces, and the blood vessel segments are constructed sequentially until the entire microvascular network is established, as shown in Figure S1. The normal model contains 47 straight segments, and the diameter range of the lumen is 4–9 μm. The entire network has seven inlets and three outlets, as shown in Figure 1. The stenosis model is based on the normal microvascular model and constructed by narrowing the lumen of local vessel according to Hill et al.'s [19] research. In the stenosis model, eight vessel segments are stenotic. The stenosis is located at the proximal end of the first 5 μm diameter vessel at the entry bifurcation, which simulates the position of the terminal SMC on the capillary, as shown in Figure 2(b). The length of the stenosis is 10 μm, and the diameter of the lumen becomes 2.5 μm. According to Amki et al.'s [21] research, about 20%–30% of the capillaries in the infarct core and penumbra are still occluded after the recanalization of large blood vessels. As shown in Figure 2(c), based on the stenosis model, the occlusion model blocks four

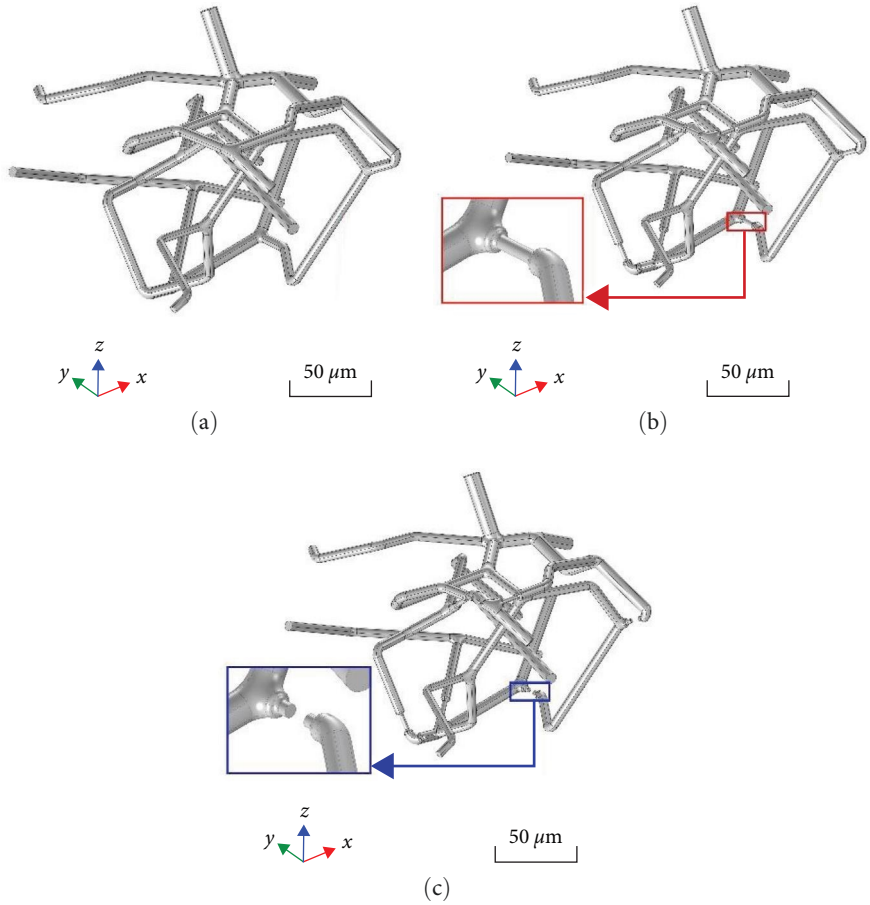

Figure 2: Geometric models used in the CFD simulation. Geometry of the normal model (a). Geometry of the stenosis model, inside the red frame is an enlarged view of the stenosis of the vessel. There are eight stenosis sites in the stenosis model (b). Geometry of the occlusion model, inside the blue frame is an enlarged view of the occlusion of the vessel. The occlusion model blocks four stenoses to simulate the narrow lumen being blocked by cells based on the stenosis model. There are four occlusions in the occlusion model (c).

stenoses to simulate the narrow lumen being blocked by cells. There are four blockages in the occlusion model.

After building the geometric model of microvascular, meshes are built for performing the CFD simulation. Since the geometry is complicated, an autogenerated tetrahedral mesh is used in the simulation, as shown in Figure 1. To ensure that the results are independent of the meshing parameters, we perform a mesh independence analysis. The mesh is refined four times, ranging from 38,217 tetrahedrons for the coarse mesh to 552,052 tetrahedrons for the fine mesh. We stop refinement when the difference in the total amount of binding NPs between two consecutive mesh refinements in the same model is below 2%. Finally, the number of mesh elements is, respectively, 203,456 for normal model, 271,880 for stenosis model, and 270,457 for occlusion model. The averaged quality of mesh is 0.68, which is good enough to ensure the convergence of computation. Additionally, the boundary layer is created for the vessel wall, which is also detailed in Figure 1.

2.2. Blood Flow Modeling

2.2.1. Fluid Properties. Blood plasma is simulated flowing in the network and treated as a Newtonian fluid with a density of 1,025 kg/m^3. The viscosity of blood plasma is 1.2 mPa·s at 37°C.

2.2.2. Governing Equations. Since the blood plasma can be treated as an incompressible liquid, the governing equations including the continuity equation and Navier–Stokes equation are numerically solved in this work:

$$\frac{\partial \rho}{\partial t} + \nabla \cdot (\rho \mathbf{u}) = 0\,, \tag{1}$$

$$\rho \frac{\partial \mathbf{u}}{\partial t} + \rho(\mathbf{u} \cdot \nabla)\mathbf{u} = \nabla \cdot (-p\mathbf{I} + \mathbf{K}) + \mathbf{F}, \tag{2}$$

where ρ is the density of blood plasma (kg/m^3), $\mathbf{u}$ is the velocity vector (m/s), p is the pressure of blood plasma (Pa) $\mathbf{I}$ is unit tensor, $\mathbf{F}$ is the volume force vector (N/m^3), $\mathbf{K}$ is the viscous stress tensor (Pa). For incompressible flow, $\mathbf{K}$ can be calculated by the velocity gradient, $\mathbf{K} = \mu(\nabla \mathbf{u} + \nabla \mathbf{u}^{\mathrm{T}})$, and μ is the fluid viscosity (Pa·s).

2.2.3. Boundary Conditions. The combination of velocity inlet and pressure outlet is utilized in this simulation, which

Table 1: Boundary condition of CFD simulation for normal model.

Boundary	Value
Inlet 1	2 mm/s
Inlet 2	2 mm/s
Inlet 3	1 mm/s
Inlet 4	0.5 mm/s
Inlet 5	1 mm/s
Inlet 6	3.5 mm/s
Inlet 7	1 mm/s
Outlet 1	0 Pa
Outlet 2	580 Pa
Outlet 3	181 Pa

has a good performance for convergence and is widely used in the fluid flow simulation. The flow velocity of the inlet and outlet of the normal model is consistent with the parameters in Secomb et al.'s [20] research. The velocity of inlet is set at first, and then the pressure of outlet is adjusted to ensure the blood flow rate in vessels matching the value in the literature. The inlet velocity and outlet pressure of normal model are shown in Table 1.

2.3. NP Modeling

2.3.1. Particle Properties and Release. In this study, five kinds of 100 nm NPs often used as carriers for nanodrug delivery systems are simulated, they are gold nanoparticles (AuNP), magnetic iron oxide nanoparticles (Fe_3O_4NP), silica nanoparticles (SiO_2NP), poly (lactic-co-glycolic acid) nanoparticles (PLGANP), and liposome. The densities of these five NPs are AuNP 19.32 g/cm^3, Fe_3O_4NP 5.17 g/cm^3, SiO_2NP 2.4 g/cm^3, PLGANP 1.3 g/cm^3, and liposome 1 g/cm^3, which can cover the density range of most nanocarriers. In order to explore the effect of particle size on NP delivery, six sizes of Fe_3O_4NP are simulated in this study, which are set as 20, 50, 100, 200, 500, and 1,000 nm, respectively. NPs are microscopic particles on the nanometer scale. It is defined as particles smaller than 100 nm in at least one dimension. However, some NPs used in the field of biomedicine are larger than 100 nm, especially the complexly modified NPs, whose hydrodynamic size often exceeds 100 nm. Thus, the diameter of NPs simulated in this study is not limited to below 100 nm. These NPs are modeled as spherical solid particles. In the simulation, each type of particle is randomly released at the inlet every 0.01 s, 100 particles per release, for a total of 10 releases.

2.3.2. Force on the Particle. The motion of NPs in blood plasma can be described by the following equation:

$$m_{\mathrm{p}} \frac{d^2\mathbf{x}}{dt^2} = \mathbf{F_p}, \tag{3}$$

where $\mathbf{x}$ is the position of the particle, m_{p} is the particle mass, and $\mathbf{F_p}$ is the sum of all forces acting on the particle.

In this study, the NPs are subjected to drag force, Brownian force, and volume repulsion by RBCs. Since the influence of gravity and lift force on NPs is small compared to the drag force, and the number of NPs released in blood vessels is small, the effects of gravity, lift, and interparticle collisions are ignored. The drag force $\mathbf{F}_{\mathrm{D}}$ is defined as follows:

$$\mathbf{F}_{\mathrm{D}} = \left(\frac{1}{\tau_{\mathrm{p}}}\right) m_{\mathrm{p}}(\mathbf{u} - \mathbf{v}), \tag{4}$$

where τ_{p} is the particle velocity response time (s), $\mathbf{v}$ is the velocity of the particle (m/s), and $\mathbf{u}$ is the fluid velocity (m/s).

As the particle Reynolds number is very low, the Stokes drag law is applied in the simulation. In the Stokes drag law, the velocity response time is calculated as follows:

$$\tau_{\mathrm{p}} = \frac{\rho_{\mathrm{p}} d_{\mathrm{p}}^2}{18\,\mu}, \tag{5}$$

where μ is the fluid viscosity (Pa·s), ρ_{p} is the particle density (kg/m^3), and d_{p} is the particle diameter (m).

Besides the drag force, Brownian force is considered in the simulation. It originates from the unbalanced force exerted by surrounding fluid molecules [22] and can be expressed in a drag analogy force model under a Lagrangian reference frame. The Brownian force $\mathrm{F_B}$ is defined as follows:

$$\mathrm{F_B} = \zeta \sqrt{\frac{6\pi k_{\mathrm{B}} \mu T d_{\mathrm{p}}}{\Delta t}}, \tag{6}$$

where Δt is the time step in the calculation (s), T is the absolute fluid temperature (K), k_{B} is the Boltzmann constant, and ζ is a normally distributed random number with a mean of zero and unit variance. The random direction of the Brownian force is accounted for by evaluating both the x and y components of $\mathrm{F_B}$ at each time step using independent values of ζ in the two directions [23]. It means that a particle will randomly walk due to the Brownian force, while the expectation of final particle position is the original position (ζ with a mean of zero) and the mean squared displacement of particles obeys a normal distribution (ζ with unit variance).

RBCs deform as they flow through capillaries between 3 and 13 μm in diameter and travel in a single line [24]. However, the deformability of RBCs is affected by various pathological conditions or as normal RBC aging, possibly resulting in loss of deformability [25, 26]. Given that the exact geometry of the RBCs in the capillaries is not known and for the purpose of simplifying the model. In this study, instead of modeling the complex geometry of the RBCs, the interaction between RBCs and NPs is modeled by Morse potential, so as to simulate the volume repulsion effect of RBCs on NPs [17, 18, 27]. The Morse potential is given as follows:

$$\phi(R) = D_e\left[e^{2\beta(R_0 - R)} - 2e^{\beta(R_0 - R)}\right], \tag{7}$$

$$f(R) = -\frac{\partial \phi(R)}{\partial R} = 2D_e\beta\left[e^{2\beta(R_0-R)} - e^{\beta(R_0-R)}\right], \quad (8)$$

where R is the distance between the NP and the RBC surface, R_0 is an equilibrium distance in which the interaction forces are equal to zero, D_e is the potential well depth, and β is a scaling factor that controls the potential well width. RBCs are released every 0.01 s at the center of the inlet, 0.005 s earlier than the release of the NPs.

2.3.3. Particles Binding Probability Function. As the first line of defense of the blood–brain barrier, endothelial cells regulate adhesion molecules after ischemia, which promotes the rolling, and firm adhesion of both leukocytes and platelets [28]. Intercellular adhesion molecule-1 (ICAM-1) as an important adhesion molecule that mediates the adhesion reaction is considered pivotal in neutrophil recruitment. In this study, the dynamic adhesion model proposed by Decuzzi and Ferrari [29] is used to simulate the binding of ICAM-1 antibody (abICAM)-modified NPs to ICAM-1 on the surface of endothelial cells. When the distance between the NP and the blood vessel wall is close enough, the abICAM on the surface of the NP can interact with the ICAM-1 on endothelial cells to form a bond. This process is stochastic in nature and given the usually small number of molecules involved, the probabilistic kinetic formulation of McQuarrie is used to estimate the likelihood of bond formation. The probability of binding P_a is defined as the probability of having at least one close ligand–receptor bond. Decuzzi and Ferrari's [29] study shows that for spherical particles, the adhesion strength increases as the surface density of receptor m_r and ligand m_l increases and the association coefficient K_a^0 increases. Among the three aforementioned parameters involved in the increase in the strength of adhesion of particles to a substrate, the values for K_a^0 and m_r are selected and used in regard to the surface pathology of the endothelial cells after ischemia and intrinsic properties of specific ligand–receptor pairs, as described in the research methods of Shamloo et al. [30]. Hence, the term P_a/m_l is evaluated in the adhesive dynamic simulations here, as follows:

$$P_a/m_l = m_r K_a^0 \pi r_0^2 \exp\left[-\frac{\lambda d\mu S}{2k_B T r_0^2 m_r}\left[6\left(d/2+\delta_{eq}\right)F^S + 2\frac{d^2}{r_0}T^S\right]\right], r_0^2 = d_p^2\left[\frac{1}{4} - \left(\frac{1}{2} - \frac{\left(h_0-\delta_{eq}\right)}{d_p}\right)^2\right], \quad (9)$$

where m_r and m_l are the surface density of the receptor and the surface density of the ligand, respectively. K_a^0 is the association constant at zero load of the ligand–receptor pair. r_0 is the radius of the circular section of the spheroid situated at a separation distance h_0 from the substrate. λ is a characteristic length of the ligand–receptor bond. The μS is the shear stress at the wall. h_0 is the maximum distance of the particle from the vessel wall at which a specific bond can take place. δ_{eq} is the equilibrium separation distance between the spheroidal particle and the vessel substrate.

F^S and T^S are the function coefficients of the hydrodynamic aspect ratio of the particle ($\gamma = a/b$):

$$F^S = 1 + (1.736 - 0.138\gamma + 0.128\gamma^2 + 0.09\gamma^3)e^{-\gamma}, \quad (10)$$

$$T^S = 1 + (-20.50 + 46.50\gamma - 35.10\gamma^2 + 8.95\gamma^3)e^{-\gamma}. \quad (11)$$

For spherical particle, $a = b$, $\gamma = 1$, that is $F^S \approx 1.668$ and $T^S \approx 0.944$ [29].

The kinetic rates of the interaction between abICAM and ICAM-1 and parameters related to dynamic adhesion are obtained from Maul et al.'s [31] research. In addition, in order to study the independent effect of ligand–receptor pair affinity on NP binding, the order of magnitude of the association constant K_a^0 (equal to K_f^0/K_r^0) of abICAM : ICAM pair is changed while keeping other parameters unchanged. The values for relevant parameters used in this study are given in Table 2.

Table 2: The parameters used in the particle tracing for fluid flow.

Expression	Value
r_0 for RBC–NP interaction (μm)	1.5
D_e for RBC–NP interaction (μJ/m^2) [27]	1.0
03B2 for RBC–NP interaction (μm^{-1}) [27]	3.84
Intrinsic forward kinetic rate K_f^0 (s^{-1}) [31]	1.15×10^5
Intrinsic reverse kinetic rate K_r^0 (s^{-1}) [31]	1.13×10^{-4}
Equilibrium bond length δ_{eq} (nm) [31]	50
Reactive compliance λ(Å) [31]	0.21
Boltzmann's constant k_B (J/K) [31]	1.3806×10^{-23}
Surface density of receptors m_r (m^{-2}) [41]	2.7×10^{15}
Temperature T (K) [31]	310.15

The procedure of the simulation is shown in Figure 3. All simulations are performed using COMSOL Multiphysics®. The iterative coupled solver is chosen for flow field simulation and the direct segregated solver is utilized for particle tracking simulation. The simulations are run with an adaptive time step up to 0.001 s until all the particles leave the fluid domain. Relative tolerance in the simulation is 1×10^{-5}.

2.4. Statistics. All cases are run independently three times. After testing for normality and homogeneity of variance, data are analyzed using the two-way ANOVA test followed by Tukey's multiple comparisons. p value less than 0.05 is considered statistically significant. All statistics are performed on GraphPad Prism 8.0.

3. Results

3.1. Changes in Hemodynamics and RBC Distribution. The average flow velocity, pressure, and shear rate of the normal model were 1.56 mm/s, 402.36 Pa, and 1,479 s^{-1}, respectively. The average flow velocity and pressure of the stenosis model

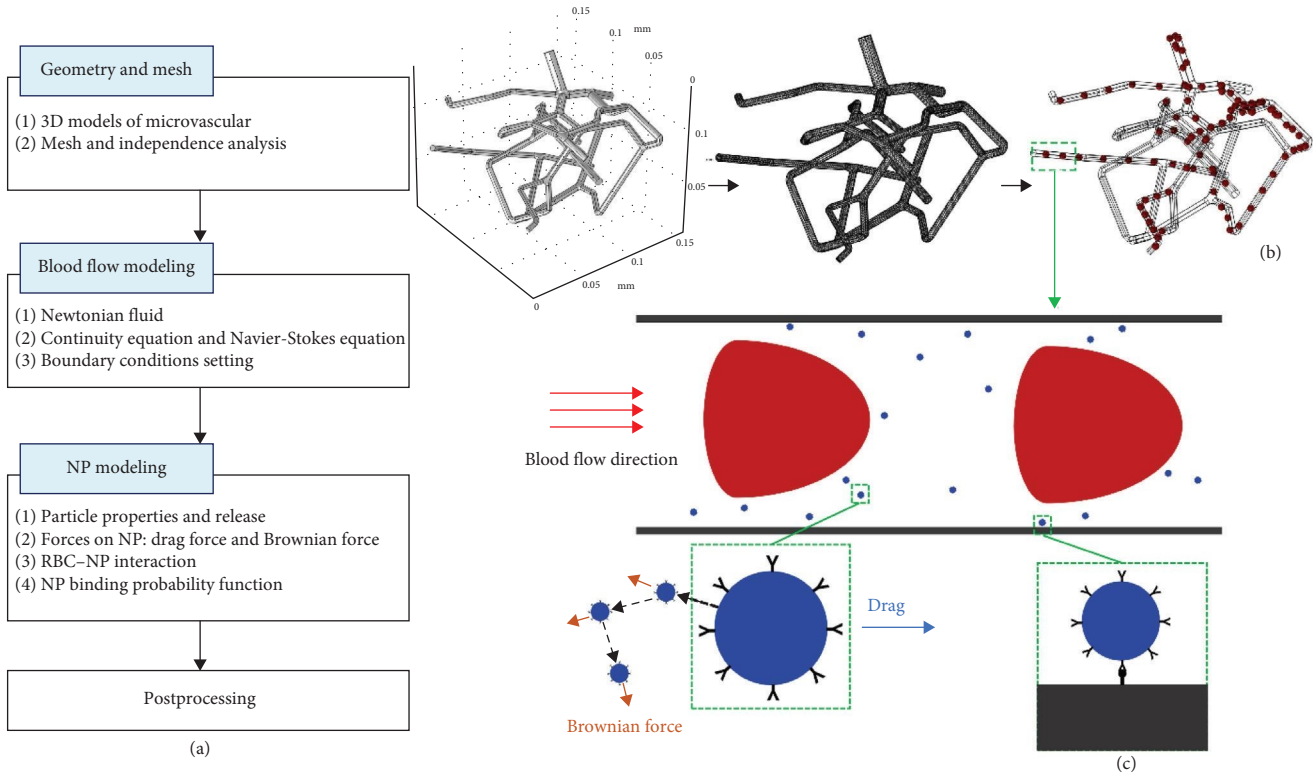

Figure 3: Schematic diagram of method. Flowchart of numerical simulation (a). Geometry to mesh, then to simulation results (b). Local enlarged view of microvascular and schematic diagram of force and modification of NPs (c).

were 1.57 mm/s and 486.39 Pa. The maximum flow velocity and pressure at the stenosis in stenosis model were 14.78 mm/s and 1,128.7 Pa. In the stenosis model, the average shear rate was 1,486 s^{-1} (excluding the narrow segment), and the average shear rate of the narrow segment was 2,580 s^{-1}. The average flow velocity and pressure of the occlusion model were 1.46 mm/s and 583.63 Pa. The maximum flow velocity and pressure at the stenosis in occlusion model were 32.19 mm/s and 1,765.8 Pa. In the occlusion model, the average shear rate was 1,311 s^{-1} (excluding the narrow segment), and the average shear rate of the narrow segment was 4,478 s^{-1}.

RBCs were released every 0.01 s at each inlet, that was, seven RBCs were released into the microvascular every 0.01 s. The distribution of RBCs in microvascular was heterogeneous, and changes in hemodynamics caused the distribution of RBCs in the three models to be different, as shown in Figures 4(c), 4(g), and 4(k). The distribution of RBCs in the normal model was relatively uniform, while the distribution of RBCs in the occlusion model was uneven and some microvascular segments showed high hematocrit.

3.2. The Effect of NP Properties on Delivery

3.2.1. Size. All three models showed that the 20 nm NPs bond the most and the 1,000 nm NPs bond the least. According to the order of particle size from small to large, the total amount of binding NPs gradually decreased, as shown in Figure 5. Comparing the total amount of binding NPs in the three models of different size, the results showed that the stenosis model had the most binding at the 20, 50, 100, and 200 nm size, but there was no statistical difference between the groups. At 500 and 1,000 nm size, the occlusion model bonds the most (p values < 0.05). The result is display in Table S1. Subsequently, the percentage of NPs bound to stenotic vessel segments as a percentage of the total amount of binding NPs were evaluated in the stenosis model and the occlusion model, respectively, as shown in Figure 6. In the stenosis model, 1,000 nm NPs showed the highest binding percentage. In the occlusion model, 20 nm NPs had the least binding percentage in the narrow segment, while 1,000 nm NPs had the highest binding percentage. The percentage of binding number attached to the stenotic vessel segments increased with particle size.

3.2.2. Density. There was no obvious rule to follow in the total amount of binding NPs with different densities in the three models, as shown in Figure 7. Comparing the total binding amount in the three models at each density, only three groups were statistically different, which were SiO_2NP between stenosis model and occlusion model, PLGANP between normal model and occlusion model, and Liposome between normal model and occlusion model, as shown in Table S2. Likewise, the percentage of NPs binding to stenotic vessel segments was evaluated. As shown in Figure 8, there was no obvious rule to follow in the binding percentage of NPs of each density on the stenotic vessel segments.

3.3. Sensitivity to the Binding Affinity of the Targeted Receptor. To explore the effect of targeted receptor binding affinity on NP binding, the magnitude of K_a^0 value of abICAM:ICAM

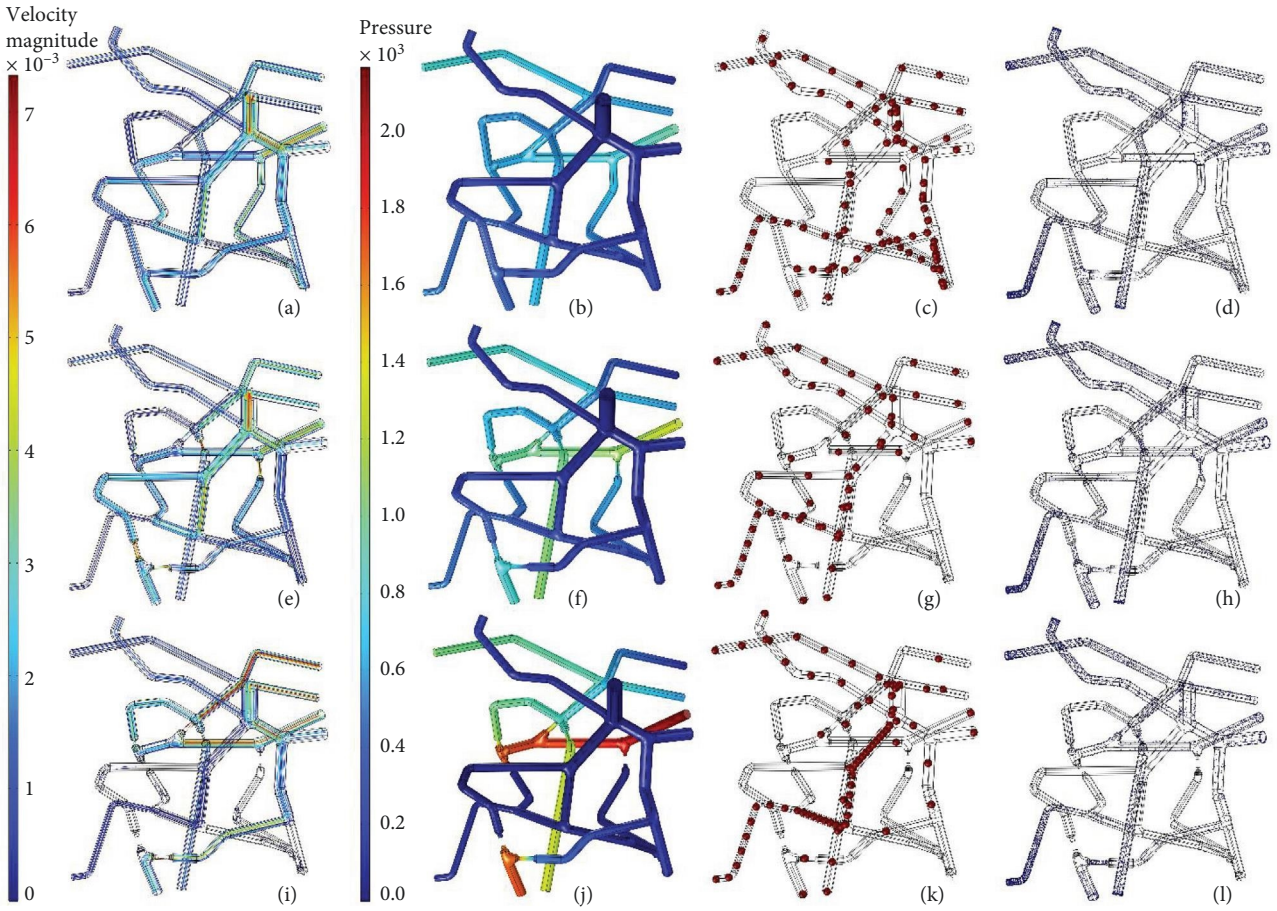

Figure 4: Schematic illustration of the flow field changes and NP distribution in three models. Each row, from top to bottom, is the normal model, the stenosis model, and the occlusion model. The first column is the average velocity streamline nephogram of three models, the unit is m/s (a, e, i). The second column is the average pressure nephogram of three models, the unit is Pa (b, f, j). The third column is the RBC distribution map of three models (c, g, k), the fourth column is the schematic diagram of the NP distribution in three models (d, h, l).

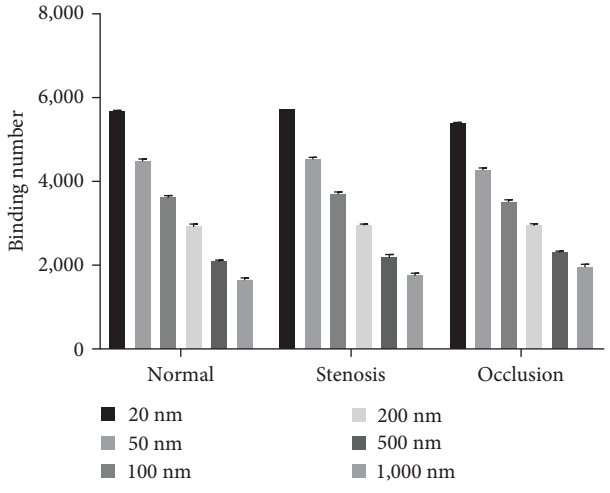

Figure 5: The total amount of binding NPs with different sizes.

pairs was artificially varied for simulation. In this study, six orders of magnitude of K_a^0 were simulated, that was, K_a^0 is equal to 0.001, 0.01, 0.1, 1, 10, and 1.018×10^9 (the real K_a^0 value). The simulation results showed that when the K_a^0 value was less than 0.1, the binding number of NPs was proportional to the value of K_a^0, while the K_a^0 value exceeded 0.1, the binding number of NPs did not change with the K_a^0 value. That was, K_a^0 value of 0.1 was the independent maximum threshold for the binding of abICAM-modified NPs to the vessel wall, as shown in Figure S2.

3.4. The Force on NP Delivery

3.4.1. Interaction with RBC. To explore the effect of RBCs on NP delivery, the total amount of binding NPs with different sizes was compared in the presence or absence of RBCs. All three models showed that NPs bond more in the presence of RBCs. In addition, NPs with larger particle size tended to increase less than smaller particle size in the presence of RBCs, as shown in Figure 9. The 20 nm NPs increased the most, while the 1,000 nm NPs increased the least.

3.4.2. Drag Force and Brownian Force. It was obvious that the drag force drove the NPs forward in blood vessels, and the Brownian force made the NPs diffuse in all directions. The simulation results showed that in the absence of Brownian forces, NPs rarely bond to the vessel wall in the normal model, while in the stenosis model and occlusion model, NPs were

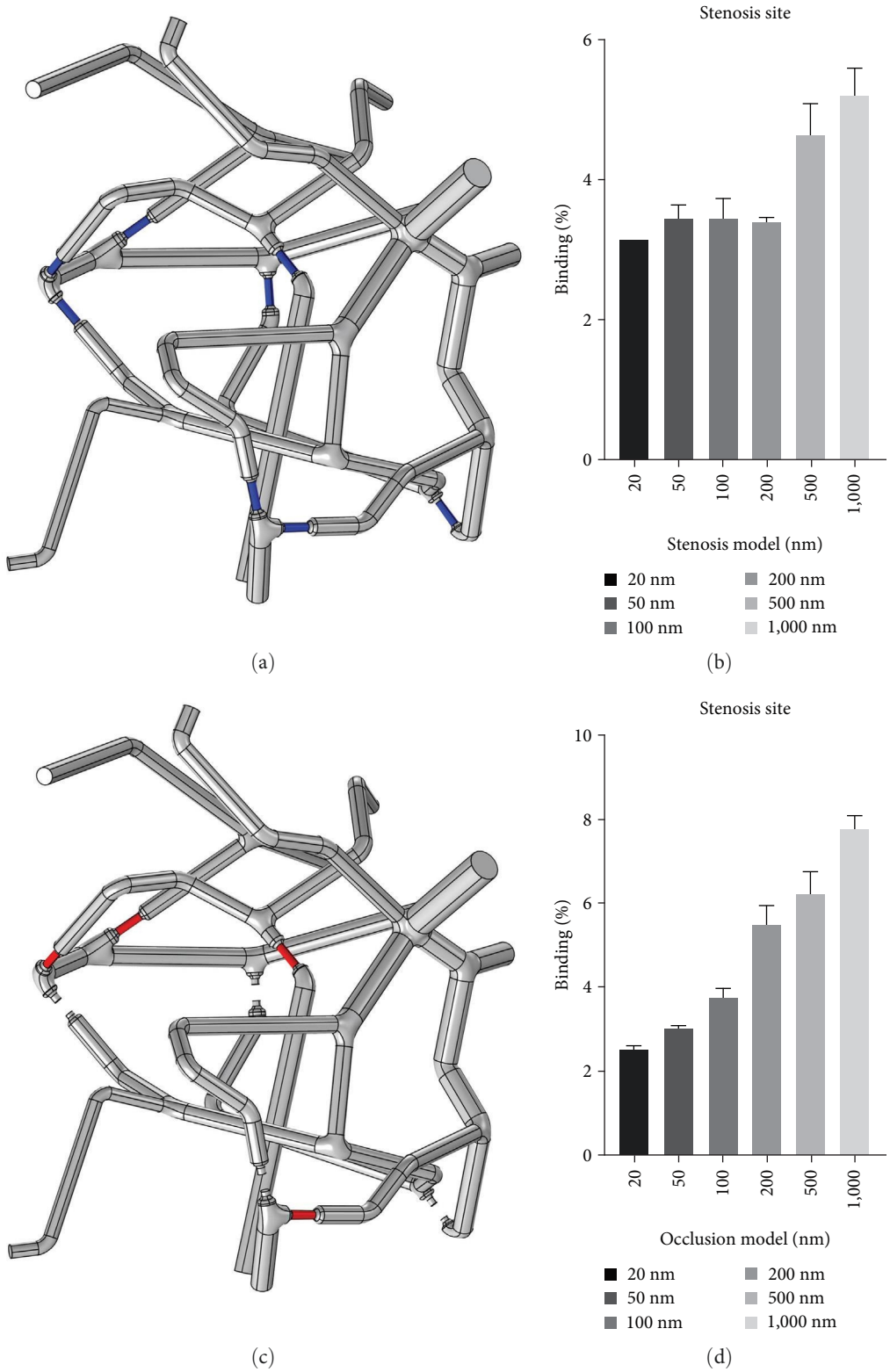

Figure 6: Binding percentage of NPs with different sizes on the stenotic vessel segment. Eight narrow segments in the stenosis model are highlighted in blue (a). The number of NPs bound to the narrow segment as a percentage of the total amount of binding NPs in stenosis model (b). Four narrow segments in the occlusion model are highlighted in red (c). The number of NPs bound to the narrow segment as a percentage of the total amount of binding NPs in occlusion model (d).

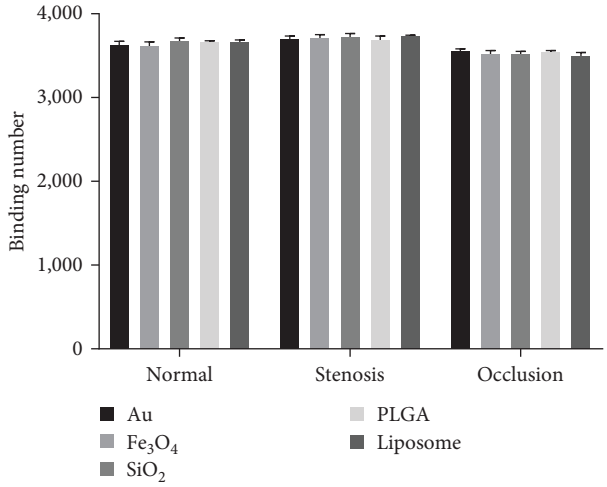

Figure 7: The total amount of binding NPs with different densities.

mainly bound to the narrow segments, as shown in Figure 10. It could be seen that the Brownian force was the main force driving the NPs to approach the vessel wall. In the absence of the Brownian force, NPs had a very small probability of approaching the vessel wall for receptor–ligand binding.

4. Discussion

After cerebral ischemia, a series of pathological changes occur in the microvascular. Morphologically, the capillary lumen is partially narrowed and then occluded, which induces hemodynamic changes [19]. As shown in Figure 4, local stenosis and occlusion of cerebral microvasculature after ischemia alter the velocity, pressure, and shear rate of the entire flow field. Correspondingly, NPs delivery is affected, which is especially evident at the stenosis. In general, small-sized NPs are more likely to be delivered to and attached to the vessel wall than large-sized NPs, and the delivery ability gradually weakens with the increase of particle size. This conclusion is consistent with the findings of Takeishi and Imai's [32] study. However, some studies show that submicron particles or microparticles (MPs) are more accessible to the vessel wall than NPs because of their margination properties [27, 33, 34]. The reason for the contradictory conclusion is mainly that the diameters of simulated microvascular are different. The vascular model studied by Takeishi and Imai [32] belongs to capillaries (microvascular diameter/RBC diameter ≤ 1.25), while the simulated microvascular in the studies that MP is more effective than NP in approaching the vessel wall belonged to relatively large microvascular, not capillaries. The microvascular network in this study belongs to capillaries, so NPs with small size exhibit higher delivery efficiency in general. Selecting the appropriate delivery particles according to the diameter of the targeted microvascular can greatly improve the delivery efficiency.

A previous study shows that density is an important factor affecting NP delivery within microvascular. Toy et al. [35] evaluated the effect of critical physical characteristics such as the particle shape, size, and density on a NP's tendency to marginalize toward vessel walls in microvascular using a vitro model. They find that density plays an important role in the vessel margination of NPs in the microvascular, NPs with low density are more likely to approach vessel margins. However, the results of this study show no statistical difference in the number or percentage of NPs with different densities attached on normal or diseased vessel walls. It is due to the fact that the Reynolds number of NPs moving in capillaries is very small, and the inertial effect of the NPs is negligible, so density has no significant effect on NP delivery. The reason why Toy et al.'s [35] study concludes that density is an important factor affecting the marginalization of NP vessels, considering that the vitro model they studied is similar to arterioles or venules, and the viscosity of nanofluids may be lower than blood, so that the inertial force of the NPs becomes dominant.

In addition to the properties of NPs themselves, the ligands modified on the NPs are another important factor that determines the delivery efficiency. The selection of appropriate ligands to modify NPs is critical to improve the targeting ability of NPs, which significantly influence the binding strength between the NPs and vessel wall [36, 37]. In this study, the delivery of NPs under different binding strength is evaluated by changing the order of magnitude of the association coefficient K_a^0 in Equation (10). It is found that the total amount of binding NPs is linearly proportional to the magnitude of the K_a^0 value, and there exists a threshold.

RBCs are deformed as they flow from the large vessels into the microvascular. In the capillaries, they pass in a parachute-like single file. Zhao et al. [34] found that in the capillary-level channels, the volume exclusion of RBCs becomes the main mechanism of particle marginalization, which occurs at a much shorter time scale than the migration in large channels. Different from directly establishing the geometric model of RBCs in the lumen, this study realizes the volume repulsion of RBCs to NPs by setting the range of action of RBCs on NPs, that is, taking the center of RBCs as the origin and forming a potential field to interact with NPs. Morse potential is used to simulate the repulsion between RBC–RBC and RBC–NP [38, 39]. By ignoring the deformation of RBCs in the flow, it is efficient to simulate the particle delivery in large-scale 3D capillary networks, given the shape and flow of RBCs in capillaries. The results in Figure 9 demonstrate that the presence of RBCs increases the total amount of binding NPs in various sizes. This phenomenon is attributed to the volume exclusion effect of RBCs on NPs at the capillary level, which is consistent with the findings of Zhao et al. [34].

The movement of NP in the microvascular is mainly affected by drag force and Brownian force. The drag force is the predominant force that drives the NPs moving axially. The Brownian force is an important force for the movement of NPs, which dominated the radial movement and played an important role in the movement of NPs to the vicinity of the vessel wall [39, 40]. The Brownian motion of small-sized NPs is stronger than that of large-sized NPs, which makes

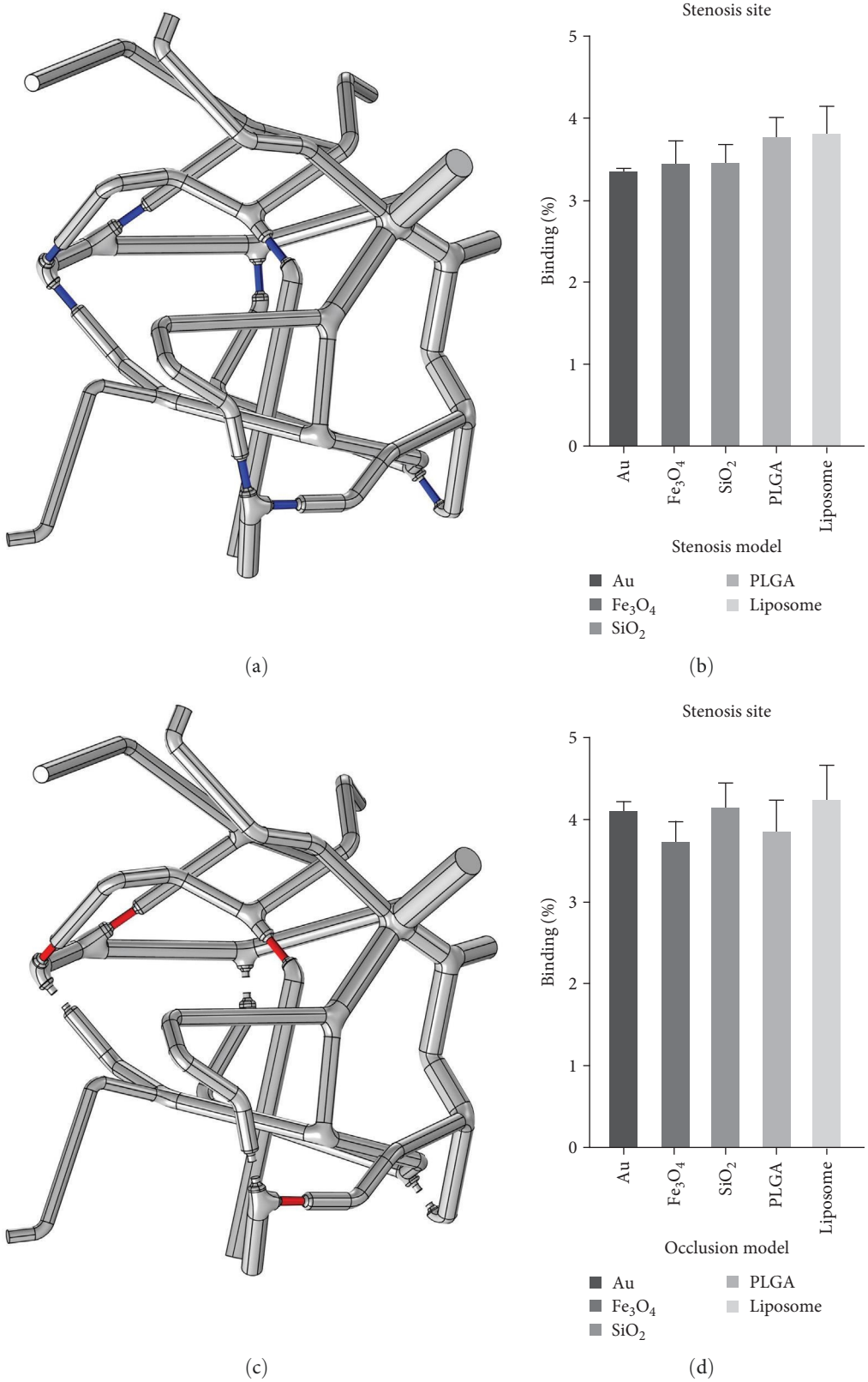

Figure 8: Binding percentage of NPs with different densities on the stenotic vessel segment. Eight narrow segments in the stenosis model are highlighted in blue (a). The number of NPs bound to the narrow segment as a percentage of the total amount of binding NPs in stenosis model (b). Four narrow segments in the occlusion model are highlighted in red (c). The number of NPs bound to the narrow segment as a percentage of the total amount of binding NPs in occlusion model (d).

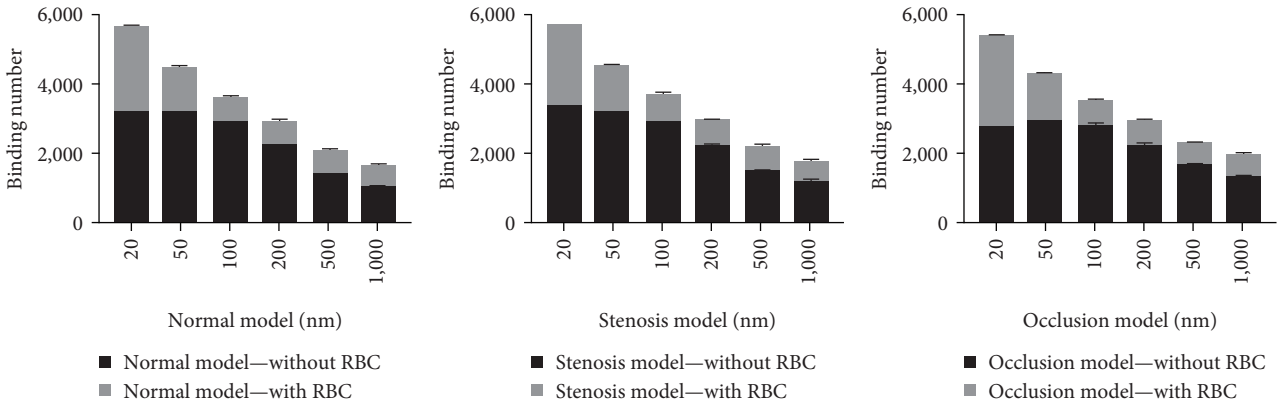

Figure 9: The effect of RBCs on the delivery of NPs with different sizes in three models.

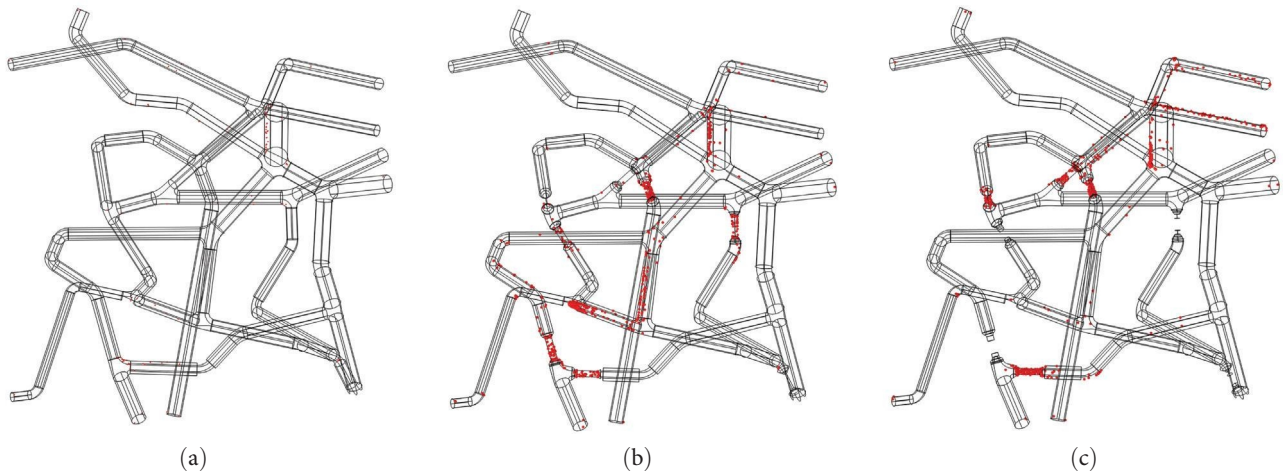

Figure 10: The binding of NPs without the Brownian force to the vessel wall in the normal model (a), the stenosis model (b), and occlusion model (c).

small-sized NPs more likely to approach the vessel wall. However, in narrow segments, large-size NPs show a higher percentage of binding. Although the Brownian motion of large-sized NPs is smaller than that of small-sized NPs, large-sized NPs can be pushed by RBCs more strongly [27] and close to the vessel wall where the stenosis occurs, so they are more likely to bind to stenosis site. Since the fluid velocity in the blocked vessel is zero, there is no influx of NPs, as shown in Figure 4. It is essential to treat the no-reflow phenomenon after reperfusion by various means to dilate the stenotic blood vessels as soon as possible to prevent the occlusion.

This study has simulated NPs passing through many divergent and convergent bifurcations in the microvascular considered as a complex network geometry. At diverging bifurcations, the hematocrit is distributed unevenly, with a higher hematocrit normally entering the branch with higher flow. The constructed microvascular shows considerable heterogeneity, which cannot be simulated by simple microvascular models. Compared with building a simple microvascular model, simulation using microvascular constructed based on real data can more systematically illustrate the law of NP delivery. In addition, this study models the microvascular based on the pathological changes after cerebral ischemia, and the simulation results obtained can guide the application of nanomedicines in cerebral ischemia. This study systematically reveals the mechanisms of delivery of NPs with different sizes and densities within ischemic capillaries. Different-sized NPs should be chosen for different therapeutic purposes when using as drug carriers. For example, large-sized NPs are suitable as drug carriers for the treatment of microvascular stenosis, such as alleviating terminal SMC contraction or microthrombosis; small-sized NPs are suitable as drug carriers, such as neuroprotective agents, that need to be delivered to ischemic brain tissue as much as possible. Researchers can select suitable NP carriers for research and development based on their therapeutic goals.

However, this study has some limitations. First of all, the microvascular network in this study is from the cortex of one rat. More and larger microvascular networks need to be established for simulation in the future. Second, the simulation methods and conclusions of this study are applicable to capillary networks, and microvascular networks of arterioles and venules require other methods designed according to blood rheology. In addition, many other factors that may

affect the microvascular delivery and binding of NPs are not included in this study, such as NP morphology, surface charge. In the future, we will include other parameters such as the shape and surface properties of NPs in the scope of research and establish larger scale microvascular networks for simulation, so as to obtain more results to help design nanodrug delivery systems related to cerebral ischemia. In summary, this study numerically simulates the delivery of NPs in microvascular after cerebral ischemia, helping researchers design nanomedicines for the treatment of cerebral ischemia.

5. Conclusion

In this study, 3D models of cerebral microvascular based on ischemic pathological changes are constructed and CFD is used to simulate the blood flow and the delivery of NPs. Overall, the size and density of the NPs, the force exerted on NPs, the binding affinity of the modified ligand on the NP to the target receptor, and the presence of RBCs all have an impact on the intravascular delivery of NPs. Small-sized NPs show high delivery efficiency in microvascular, while large-sized NPs show high binding probability at stenotic sites. Small-sized nanocarriers are suitable for drugs that need to be delivered to ischemic brain tissue as much as possible, such as neuroprotective agents, while large-sized nanocarriers are suitable for delivering drugs that target microvascular stenosis, such as alleviating terminal SMCs constricting, or microthrombosis. The density of nanocarriers has a negligible effect on delivery. The microvascular NPs delivery model constructed in this study can provide ideas for researchers to design nanomedicines more suitable for the diagnosis and treatment of cerebral ischemia.

Data Availability

The simulation cases used to support the findings of this study are supplied by Weiwu Yao under license and so cannot be made freely available. Requests for access to these data should be made to Weiwu Yao, yaoweiwuhuan@163.com.

Conflicts of Interest

The authors declare that the research was conducted in the absence of any commercial or financial relationships that could be construed as a potential conflicts of interest.

Authors' Contributions

Peiqian Chen contributed to design the research, analyze data, and write the manuscript. Bing Dong contributed to carry out simulations. Weiwu Yao contributed to supervise and funding the project.

Acknowledgments

This work is supported by the National Natural Science Foundation of China (No. 81771790).

Supplementary Materials

This supplementary material includes statistical results of the total amount of binding NPs with different sizes and densities in the three models, the schematic diagram of the steps to build the model, and the statistical graphs of the total amount of binding NPs with different K_a^0 values. (*Supplementary Materials*)

References

[1] V. L. Feigin, B. A. Stark, C. O. Johnson et al., "Global, regional, and national burden of stroke and its risk factors, 1990–2019: a systematic analysis for the global burden of disease study 2019," *The Lancet Neurology*, vol. 20, no. 10, pp. 795–820, 2021.

[2] M. G. Mosconi and M. Paciaroni, "Treatments in ischemic stroke: current and future," *European Neurology*, vol. 85, no. 5, pp. 349–366, 2022.

[3] F. Şen and G. Gökağaç, "Improving catalytic efficiency in the methanol oxidation reaction by inserting Ru in face-centered cubic Pt nanoparticles prepared by a new surfactant, *tert*-octanethiol," *Energy & Fuels*, vol. 22, no. 3, pp. 1858–1864, 2008.

[4] V. K. Sangwan and M. C. Hersam, "Neuromorphic nanoelectronic materials," *Nature Nanotechnology*, vol. 15, no. 7, pp. 517–528, 2020.

[5] P. J. J. Alvarez, C. K. Chan, M. Elimelech, N. J. Halas, and D. Villagrán, "Emerging opportunities for nanotechnology to enhance water security," *Nature Nanotechnology*, vol. 13, no. 8, pp. 634–641, 2018.

[6] T. Gur, I. Meydan, H. Seckin, M. Bekmezci, and F. Sen, "Green synthesis, characterization and bioactivity of biogenic zinc oxide nanoparticles," *Environmental Research*, vol. 204, Article ID 111897, 2022.

[7] X. Zhao, C. Liu, J. Yu et al., "Hydrophobic multiscale cavities for high-performance and self-cleaning surface-enhanced Raman spectroscopy (SERS) sensing," *Nanophotonics*, vol. 9, no. 16, pp. 4761–4773, 2020.

[8] M. Li, J. Li, J. Chen et al., "Platelet membrane biomimetic magnetic nanocarriers for targeted delivery and *in situ* generation of nitric oxide in early ischemic stroke," *ACS Nano*, vol. 14, no. 2, pp. 2024–2035, 2020.

[9] L. Feng, C. Dou, Y. Xia et al., "Neutrophil-like cell-membrane-coated nanozyme therapy for ischemic brain damage and long-term neurological functional recovery," *ACS Nano*, vol. 15, no. 2, pp. 2263–2280, 2021.

[10] Y. Lu, C. Li, Q. Chen et al., "Microthrombus-targeting micelles for neurovascular remodeling and enhanced microcirculatory perfusion in acute ischemic stroke," *Advanced Materials*, vol. 31, no. 21, Article ID 1808361, 2019.

[11] J. Yuan, L. Li, Q. Yang et al., "Targeted treatment of ischemic stroke by bioactive nanoparticle-derived reactive oxygen species responsive and inflammation-resolving nanotherapies," *ACS Nano*, vol. 15, no. 10, pp. 16076–16094, 2021.

[12] G. Huang, J. Zang, L. He et al., "Bioactive nanoenzyme reverses oxidative damage and endoplasmic reticulum stress in neurons under ischemic stroke," *ACS Nano*, vol. 16, no. 1, pp. 431–452, 2022.

[13] T. Al Sariri and R. Penta, "Multi-scale modelling of nanoparticle delivery and heat transport in vascularised tumours," *Mathematical Medicine and Biology: A Journal of the IMA*, vol. 39, no. 4, pp. 332–367, 2022.

[14] M. R. Motaghedifar, A. Fakhar, H. Tabatabaei, and M. Mazochi, "The effect of pharmaceutical nanoparticles and atherosclerosis in aorta artery on the instable blood velocity based on numerical method," *International Journal for Numerical Methods in Biomedical Engineering*, vol. 38, no. 5, 2022.

[15] L. I. Kolitsi and S. G. Yiantsios, "Transport of nanoparticles in magnetic targeting: comparison of magnetic, diffusive and convective forces and fluxes in the microvasculature, through vascular pores and across the interstitium," *Microvascular Research*, vol. 130, Article ID 104007, 2020.

[16] J. Tan, S. Shah, A. Thomas, H. D. Ou-Yang, and Y. Liu, "The influence of size, shape and vessel geometry on nanoparticle distribution," *Microfluidics and Nanofluidics*, vol. 14, no. 1-2, pp. 77–87, 2013.

[17] Z. Liu, J. R. Clausen, R. R. Rao, and C. K. Aidun, "Nanoparticle diffusion in sheared cellular blood flow," *Journal of Fluid Mechanics*, vol. 871, pp. 636–667, 2019.

[18] K. Yue, Y. You, C. Yang, Y. Niu, and X. Zhang, "Numerical simulation of transport and adhesion of thermogenic nanocarriers in microvessels," *Soft Matter*, vol. 16, no. 45, pp. 10345–10357, 2020.

[19] R. A. Hill, L. Tong, P. Yuan, S. Murikinati, S. Gupta, and J. Grutzendler, "Regional blood flow in the normal and ischemic brain is controlled by arteriolar smooth muscle cell contractility and not by capillary pericytes," *Neuron*, vol. 87, no. 1, pp. 95–110, 2015.

[20] T. W. Secomb, R. Hsu, N. B. Beamer, and B. M. Coull, "Theoretical simulation of oxygen transport to brain by networks of microvessels: effects of oxygen supply and demand on tissue hypoxia," *Microcirculation*, vol. 7, no. 4, pp. 237–247, 2000.

[21] M. El Amki, C. Glück, N. Binder et al., "Neutrophils obstructing brain capillaries are a major cause of no-reflow in ischemic stroke," *Cell Reports*, vol. 33, no. 2, Article ID 108260, 2020.

[22] S. Dong, L. Zheng, X. Zhang, S. Wu, and B. Shen, "A new model for Brownian force and the application to simulating nanofluid flow," *Microfluidics and Nanofluidics*, vol. 16, no. 1-2, pp. 131–139, 2014.

[23] M. Kim and A. L. Zydney, "Effect of electrostatic, hydrodynamic, and Brownian forces on particle trajectories and sieving in normal flow filtration," *Journal of Colloid and Interface Science*, vol. 269, no. 2, pp. 425–431, 2004.

[24] H. Noguchi and G. Gompper, "Shape transitions of fluid vesicles and red blood cells in capillary flows," *Proceedings of the National Academy of Sciences*, vol. 102, no. 40, pp. 14159–14164, 2005.

[25] G. Barshtein, I. Pajic-Lijakovic, and A. Gural, "Deformability of stored red blood cells," *Frontiers in Physiology*, vol. 12, 2021.

[26] J. Kim, H. Y. Lee, and S. Shin, "Advances in the measurement of red blood cell deformability: a brief review," *Journal of Cellular Biotechnology*, vol. 1, no. 1, pp. 63–79, 2015.

[27] T.-R. Lee, M. Choi, A. M. Kopacz, S.-H. Yun, W. K. Liu, and P. Decuzzi, "On the near-wall accumulation of injectable particles in the microcirculation: smaller is not better," *Scientific Reports*, vol. 3, no. 1, Article ID 2079, 2013.

[28] R. Daneman and A. Prat, "The blood–brain barrier," *Cold Spring Harbor Perspectives in Biology*, vol. 7, no. 1, Article ID a020412, 2015.

[29] P. Decuzzi and M. Ferrari, "The adhesive strength of non-spherical particles mediated by specific interactions," *Biomaterials*, vol. 27, no. 30, pp. 5307–5314, 2006.

[30] A. Shamloo, A. Amani, M. Forouzandehmehr, and I. Ghoytasi, "In silico study of patient-specific magnetic drug targeting for a coronary LAD atherosclerotic plaque," *International Journal of Pharmaceutics*, vol. 559, pp. 113–129, 2019.

[31] T. M. Maul, D. D. Dudgeon, M. T. Beste et al., "Optimization of ultrasound contrast agents with computational models to improve selection of ligands and binding strength," *Biotechnology and Bioengineering*, vol. 107, no. 5, pp. 854–864, 2010.

[32] N. Takeishi and Y. Imai, "Capture of microparticles by bolus flow of red blood cells in capillaries," *Scientific Reports*, vol. 7, no. 1, 2017.

[33] K. Müller, D. A. Fedosov, and G. Gompper, "Margination of micro- and nano-particles in blood flow and its effect on drug delivery," *Scientific Reports*, vol. 4, no. 1, Article ID 4871, 2014.

[34] H. Zhao, E. S. G. Shaqfeh, and V. Narsimhan, "Shear-induced particle migration and margination in a cellular suspension," *Physics of Fluids*, vol. 24, no. 1, Article ID 011902, 2012.

[35] R. Toy, E. Hayden, C. Shoup, H. Baskaran, and E. Karathanasis, "Effect of particle size, density and shape on margination of nanoparticles in microcirculation," *Nanotechnology*, vol. 22, Article ID 115101, 2011.

[36] H. Li, J. Di, B. Peng, Y. Xu, and N. Zhang, "Surface ligand valency and immunoliposome binding: when more is not always better," *Pharmaceutical Research*, vol. 38, no. 9, pp. 1593–1600, 2021.

[37] J. B. Haun and D. A. Hammer, "Quantifying nanoparticle adhesion mediated by specific molecular interactions," *Langmuir*, vol. 24, no. 16, pp. 8821–8832, 2008.

[38] Y. Liu and W. K. Liu, "Rheology of red blood cell aggregation by computer simulation," *Journal of Computational Physics*, vol. 220, no. 1, pp. 139–154, 2006.

[39] Z. Liu, Y. Zhu, R. R. Rao, J. R. Clausen, and C. K. Aidun, "Nanoparticle transport in cellular blood flow," *Computers & Fluids*, vol. 172, pp. 609–620, 2018.

[40] G. Fullstone, J. Wood, M. Holcombe, and G. Battaglia, "Modelling the transport of nanoparticles under blood flow using an agent-based approach," *Scientific Reports*, vol. 5, no. 1, 2015.

[41] G. E. R. Weller, F. S. Villanueva, A. L. Klibanov, and W. R. Wagner, "Modulating targeted adhesion of an ultrasound contrast agent to dysfunctional endothelium," *Annals of Biomedical Engineering*, vol. 30, no. 8, pp. 1012–1019, 2002.